




**Invisible devices with natural materials designed by evolutionary optimization**Bei Wu , Shuwen Xue, Zhibin Zhang , and Huanyang Chen \**Department of Physics and Institute of Electromagnetics and Acoustics, Xiamen University, Xiamen 361005, China*

(Received 24 July 2022; accepted 28 October 2022; published 23 November 2022)

It is a longstanding dream to put on a cloak and escape from sight. Transformation optics (TO) and artificial metamaterials turn this circumstance into reality, but the requirements for inhomogeneous and anisotropic materials make it almost impossible in practical realization. Furthermore, invisibility can only be constructed at a narrow frequency regime in previous studies and depends critically on the inescapable material losses. Here, the authors propose the multifrequency isotropic invisible devices and natural hyperbolic invisible devices using realistic materials, such as microwave materials and van der Waals (vdW) materials. The inherent material losses are taken into account in the optimization process, bringing the concept of invisibility closer to realistic conditions. To verify the stability of the proposed method, full-wave numerical simulations and analytical calculations are performed, and both obtained excellent invisibility performance. Due to the combined advantages of the simple two-layer core-shell configuration and natural materials, our work provides a promising platform for fabricating invisible devices at low cost and paves the way for new implementations of intelligent photonics beyond the limitations of TO.

DOI: [10.1103/PhysRevE.106.055312](https://doi.org/10.1103/PhysRevE.106.055312)**I. INTRODUCTION**

Invisibility refers to making an object invisible to the human eye or electromagnetic (EM) detector, which is of prime significance for fundamental scientific investigations, such as in spacecraft components, military defense, and electronic shielding [1]. From a physical point of view, a cloak essentially aims to tailor the interaction of electromagnetic wave with the object to make the wavefronts remain undisturbed in the surrounding medium, as if there were no object. A common route to realize invisibility is based on TO [2–4], which is a significant tool in controlling light rays and waves arbitrarily. With the development of metamaterials, many devices designed by TO have been implemented, such as invisibility cloaks [4], carpet cloaks [5–8], optical illusion devices [9–11], field rotators [12,13], and concentrators [14,15]. Theoretically, perfect invisibility can be realized by TO, but the experimental results are largely deteriorated by bulky metamaterial compositions with anisotropic, inhomogeneous, and extreme parameters [4], making it almost impossible for practical realizations. To solve this problem, various approximations have been proposed to simplify the complexity of cloak [16,17]. For example, Cummer *et al.* [18] derived a reduced version of cloaks that may be easier to experimentally realize. Meanwhile, Schurig *et al.* [19] simplified and discretized the electromagnetic parameters of the cloaks, and performed experiment at microwave frequencies to verify the cloaking effectiveness for the first time. In 2007, Cai *et al.* used metal wires of subwavelength sizes in the radial direction embedded in a dielectric material to realize anisotropic permittivities, and achieved invisibility at optical frequen-

cies [20]. In the same year, they also suggested the use of higher-order transformations to create smooth moduli at the outer boundary of the nonmagnetic cylindrical cloak, therefore eliminating the detrimental scattering within the limit of geometric optics [21]. However, the common simplified parameter method and discretization will reduce the cloaking effect. The scattering cancellation cloaks liberalize the limitation of material, which can be designed using bulky, homogenous materials with low or negative EM constitutive parameters, such as plasmonics and metasurfaces [22,23]. When an incident wave impinges on the cloaked object, the overall scattering behavior is suppressed drastically because of the “antiphase” waves. Scattering cancellation cloaks are robust to manufacturing tolerance, and the constitutive material is easily accessible, but it only works for subwavelength objects.

Another emerging approach that can be used to design cloaks is deep learning, which depends on artificial neural networks (ANNs) for data-driven predictions. The ANNs are trained to learn the intrinsic relation between the cloak parameters (such as structure and material properties) and their scattering properties, and design the cloaks immediately after the training phase. However, the design process of ANNs is time-consuming and computationally expensive, involving hyperparameter optimization, training data generation, and extensive testing. Additionally, while the ANNs are good at interpolating complex functions from training data, their performances are reduced when extrapolating outside of the known parameter space. Theoretically, with strong computing power, the ANNs can design massive invisibility models which have irregular material parameters [24]. When it comes to the realistic conditions, the research scope is limited to the natural materials. As the input data samples fed into the ANNs are generated randomly, in which few and even no

\*kenyon@xmu.edu.cn

optical structures have great invisibility performances, leaving the ANNs with few right samples to learn from and leading to the reduced cloaking performance. For example, Ahmed *et al.* designed the acoustic cloak with size of only about half a wavelength [25], in which case the scattering behavior is weak even without cloaks. To explore efficient invisible device designs, we choose an evolutionary algorithm (EA) as the optimization technique due to its ease of implementation, efficiency in exploring a large parameter space, and ability to trace intermediate solutions. Compared with deep learning, EA avoids time-consuming data preparation and is immune to the forward-modeling error. Due to these advantages, EA has been applied to a series of optical researches [26]. For example, Conkey *et al.* focused light through turbid media in noisy environments with EA [27]. Here, we use EA to design the multifrequency isotropic invisible device and natural hyperbolic invisible device using natural materials, such as microwave materials and van der Waals (vdW) materials, which possess the advantages of omnidirection, easy fabrication and low-cost.

Hyperbolic materials are highly anisotropic optical materials which originate from one of the principal components of their electric or magnetic effective tensor having the opposite sign to the other two principal components, generating a hyperbolic type of dispersion as the isofrequency contours are hyperbolic surfaces in the wave vector space [28]. Hyperbolic media with strongly anisotropic optical properties can support deep subwavelength-scale confined electromagnetic waves (polaritons), which have the ability to support electromagnetic fields with arbitrarily high momenta [29], and thus to achieve very strong light confinement [30,31]. The hyperbolic polaritons were first discovered in thin flakes of vdW crystals, such as hexagonal boron nitride (h-BN) [32–34],  $\alpha$ -phase molybdenum trioxide ( $\alpha$ -MoO<sub>3</sub>) [35],  $\alpha$ -phase vanadium pentoxide ( $\alpha$ -V<sub>2</sub>O<sub>5</sub>) [36], and the dichalcogenide tungsten diselenide (WSe<sub>2</sub>) [37]. The vdW crystals assembled from atomically thin crystalline layers of diverse two-dimensional solids have been shown to exhibit excellent hyperbolic properties in the wavelength range from ultraviolet to terahertz [34]. They feature nanoscale localization of the electromagnetic energy [38], long polariton lifetimes [39], and superconductivity [40], which facilitates various applications such as super-scattering [41], photodiodes [42], subdiffraction imaging [43], thermal energy transfer [44], and twisted nano-optics [45]. An ambitious practical goal is to further explore the invisibility properties of vdW crystals, and some related works have been reported. For example, Hou *et al.* designed a cloak with  $\alpha$ -MoO<sub>3</sub> at Fabry-Pérot resonance frequency [46]. However, the cloak only works at a narrow frequency regime, and achieving invisibility in the Reststrahlen bands is a more challenging task, due to the imaginary angular momentum specific to the hyperbolic media. Here, we solve this problem by setting periodic metal-dielectric alternating layers to substitute the hyperbolic shell, and using the EA to optimize the equivalent structure for excellent invisibility performance.

In this work, we propose the isotropic invisible devices and hyperbolic invisible devices using natural materials that can be readily achievable for invisibility technologies. In contrast to cloaks using metasurfaces, the designed invisible devices can achieve excellent invisibility phenomena without the need

for patterning, and have the capacity to achieve multifrequency invisibility. Specifically, we search for the optimal invisible device design by a global minimum search with EA to suppress the light scattering behavior at the operating frequencies. Notably, the diameter of the designed invisible devices can reach up to two wavelengths, which is a breakthrough in size compared to the scattering cancellation cloak that is only suitable for subwavelength objects. Moreover, the designed invisible devices can achieve invisibility in a wider frequency regime, which is a progress in bandwidth compared to the TO cloak that only works at a narrow frequency regime. This framework provides a promising platform for fabricating invisible devices at low cost and fostering potential applications.

## II. MODELING MIXED EVOLUTIONARY STRATEGIES

### A. Invisible model and optimization objective

For conceptual clarity, we consider an incident transversed magnetic (TM) plane wave impinging on the cylindrical structure. The circular scatter in two dimensions (located in the  $x$ - $y$  plane) is equivalent to an ideal cylinder of infinite length along the  $z$  direction and can be effectively realized by a cylinder of finite length  $L$ , which is much larger than the operating wavelength  $\lambda$ , i.e.,  $L \gg \lambda$ . Our purpose is to make a cylindrical scatterer, indicated by the pink core in Fig. 1(a), invisible. To achieve this goal, we roll a cloaking shell round it, which can be made of any materials. The properties of the cylindrical scatterer are described by its radius  $\rho_0$  and relative permittivity  $\varepsilon_i$ , while the cloaking shell is characterized by the thickness  $T$  and the relative permittivity  $\varepsilon_{\text{cloak}}$ . The optimization objective of this work is to achieve invisibility by tuning the structure, materials and the operating wavelength of the core-shell system. The optimization procedure starts with a random population of devices, then measures how well the individual devices are invisible, and finally uses the EA to select, mutate, and breed the fittest members of the population, then uses the resultant population to repeat the process [Fig. 1(b)]. The parameters of the devices are represented by 1D floating number arrays, which enable the following operations: Tournament selection, two-point crossover, and shuffling mutation (see the Appendix for details).

### B. Optimization with the combination of transfer matrix method and evolutionary algorithm

As a measurement of the fitness of individuals in the EA optimization, we calculate the scattering cross section (SCS), e.g., the total scattered power over the intensity of the incident plane wave. The SCS of TM waves in two dimensions from the concentric cylinder can be solved analytically by following the transfer matrix method (TMM). In short, the total SCS can be expressed by  $\sigma_{SCS} = \sum_{m=-\infty}^{\infty} (2\lambda/\pi) |d_m|^2$ , where the parameter  $d_m$  is the scattering coefficient of the  $m$ th angular momentum channel and can be calculated by matching the continual boundary conditions (see the Appendix for details). In the calculation of TMM, we use the normalized parameters for operating frequency and structure, which can be scaled depending on the choice of the cylindrical scatterer. For

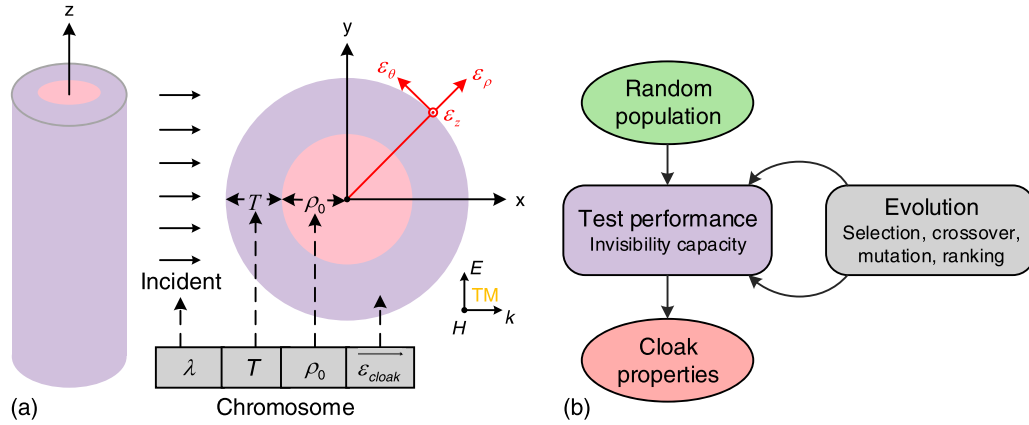


FIG. 1. (a) Schematic model used for invisible devices. Light is incident in transversed magnetic (TM) modes. The optimization variables of the operating wavelength  $\lambda$ , the radius of the cylindrical scatterer  $\rho_0$ , the thickness  $T$  and the relative permittivity  $\epsilon_{\text{cloak}}$  of the cloaking shell are decoded as a chromosome of individuals in evolutionary algorithm (EA). (b) Graphical representation of the EA scheme developed here.

example, for a 30 mm scatterer in the air, the designed invisible device perfectly works over a broad spectrum ranging from 5 to 15 GHz. Typically, the smaller the SCS, the better the invisibility performance, and the SCS is defined as the fitness of the individual in EA. Therefore, in the optimization problem we consider, the optimization objective is to minimize the fitness.

The EA runs for 10 generations, each containing 100 individual devices. The optimal population fitness for a single generation is the minimum over all 100 individuals, while the average population fitness is the average over them. Figure 2(a) shows the optimization process of EA. The red dots represent each individual, in which the corresponding abscissa value is the generation of the individual, and the ordinate value represents its fitness, e.g., the SCS of the cloaked object. The green line indicates the average fitness in each generation, while the blue line indicates the minimum fitness of the optimal individual. It implies that the optimal fitness decreases as the evolution progresses and eventually approaches saturation. Moreover, we trace the intermediate solutions and plot the results in Fig. 2(b). It shows that invisible devices designed in the individual generation are typically with strong scattering behavior, whereas the evolved designs weaken the scattering and eventually achieve invisibility.

### III. SEARCHING FOR THE OPTIMAL PARAMETERS OF INVISIBLE DEVICES

The structure and material are designed simultaneously in this system, and the invisible devices can be customized with various types of materials. Here, we give two examples of the isotropic invisible device and the hyperbolic invisible device.

#### A. Isotropic invisible device

First, we consider the case of isotropic invisible device. To demonstrate the proposed method, we consider a specific core material with the relative permittivity of  $\epsilon_i = 1.96$ , which can be realized by Rogers *RT/duroid 5880LZ* or any other materials with similar permittivity. Optical properties of invisible devices depend on the materials. However, the permittivity should not be directly used for EA, because an arbitrarily returned permittivity cannot generally be realized with real materials. Therefore, we have listed the Rogers RF materials for design, and indexed them through numbering, as shown in Table I.

The optimized cylindrical scatterer has a radius of  $\rho_0 = 20.75$  mm, and the shell has a thickness of  $T = 8.58$  mm with the Rogers *TMM 13i* ( $\epsilon_{\text{cloak}} = 12.85$ ), as depicted in Fig. 3(a). The relation between the SCS of the invisible device and the wavelength is shown in Fig. 3(b). It shows that the SCS is very small at multiple wavelengths, e.g., 20, 30, and 59 mm, proving that the multifrequency invisibility phenomena can be achieved with realistic isotropic materials. To verify the effectiveness of designed invisible device, we take the wavelength of 30mm as an example, perform full-wave numerical simulations and plot the results in Figs. 3(c)–3(h). Among them, Figs. 3(c) and 3(d) depict the  $H_z$  component diagrams of the cloaked object and the bare object under the excitation of a plane wave, while Fig. 3(e) and 3(f) depict the scattering magnetic field diagrams under the same excitation condition. It shows that the incident wave is severely distorted in the case of the bare object, indicating strong scattering behavior. In contrast, the field distribution is almost undisturbed with the presence of the cloaked object, indicating the great invisibility performance. To further explore the effectiveness

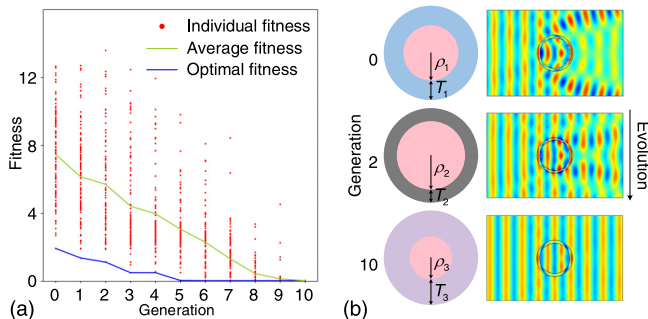


FIG. 2. Optimization process of EA for the invisible device design. (a) The dependence of population fitness on the generation. (b) Example designs from three different generations along with a snapshot from the last time step of their simulation runs.

TABLE I. Indexed Rogers RF materials.

0	1	2	3	4	5	6	...
None	RT/duroid 5880LZ ( $\epsilon = 1.96$ )	RT/duroid 5880 ( $\epsilon = 2.2$ )	RT/duroid 6002 ( $\epsilon = 2.95$ )	TMM 6 ( $\epsilon = 6$ )	RT/duroid 6010LM ( $\epsilon = 10.2$ )	TMM 13i ( $\epsilon = 12.85$ )	...

of the invisible device, the incident wave is changed into a point source, which could be equivalent to a tiny circle with a constant magnetic field, placed at the upper left corner of the cloaked object. The results shown in Fig. 3(g)–3(h) indicate that when the Rogers *TMM 13i* is rolled around the cylindrical scatterer, the  $H_z$  component diagram is almost undisturbed, while obvious scattering occurs without the cloaking shell. It has been confirmed that this method allows for the simultaneous inverse design of structure and material for the cylindrical structure to achieve multifrequency invisibility, and provides the possibility of designing two-layer invisible devices.

### B. Hyperbolic invisible device

Second, we consider the case of hyperbolic invisible device. To demonstrate the proposed method, we consider a specific core material with the relative permittivity of  $\epsilon_i = 1.44$ , which is considered as optical fiber in this work. Then we apply EA to explore the invisibility performance of h-BN, a representative vdW crystal. The material h-BN is a polar vdW crystal, thus possessing a uniaxial permittivity. Choosing  $\theta, z$  to be the in-plane directions and  $\rho$  to be the out-of-plane

direction. The permittivity ( $\epsilon_{\perp}$  for the component in the direction perpendicular to the optical axis,  $\epsilon_{\parallel}$  for parallel to the optical axis) is obtained by fitting the experimental results in Ref. [47] with a Lorentzian model and can be expressed as

$$\epsilon_l(w) = \epsilon_l(\infty) + s_{v,l} \frac{w_{v,l}^2}{w_{v,l}^2 - i\gamma_{v,l}w - w^2} \quad (l = \perp, \parallel), \quad (1)$$

where  $w$  is the angular velocity,  $s_{v,l}$  is the dimensionless coupling factor,  $w_{v,l}$  is the normal frequency of vibration, and  $\gamma_{v,l}$  is the amplitude decay rate. The specific parameters are listed in Table II. As shown in Fig. 4, there are two Reststrahlen bands in the midinfrared range: Band 1 in the range of 746 to 819  $\text{cm}^{-1}$ , where the in-plane permittivity is positive and isotropic,  $\epsilon_{\text{h-BN},\theta} = \epsilon_{\text{h-BN},z} = \epsilon_{\text{h-BN},\perp} > 0$ , and the out-of-plane permittivity is negative,  $\epsilon_{\text{h-BN},\rho} = \epsilon_{\text{h-BN},\parallel} < 0$ ; Band 2 in the range of 1372 to 1609  $\text{cm}^{-1}$ , where the in-plane permittivity is negative and isotropic,  $\epsilon_{\text{h-BN},\theta} = \epsilon_{\text{h-BN},z} = \epsilon_{\text{h-BN},\perp} < 0$ , and the out-of-plane permittivity is positive,  $\epsilon_{\text{h-BN},\rho} = \epsilon_{\text{h-BN},\parallel} > 0$ . Here, we explore the invisibility performance of h-BN in Band 1.

Due to the particularity of hyperbolic materials, the angular momentum channel  $\tilde{m} = m\sqrt{\epsilon_{\theta}/\epsilon_{\rho}}$  of the Bessel functions and Hankel functions of the first kind are imaginary (see the Appendix for details). During the optimization process, some special structures may be generated, and result in nonconvergence of the functions. Here we solve this problem by applying the effective medium theory. Specifically, the h-BN shell is substituted by a 50-periodical-layer structure, which is just an intermediate process of calculation and does not exist in fact. The equivalent relationship is as follows:

$$\begin{aligned} \epsilon_{\rho} &= (f_m/\epsilon_m + f_d/\epsilon_d)^{-1}, \\ \epsilon_{\theta} &= \epsilon_z = f_m\epsilon_m + f_d\epsilon_d, \end{aligned} \quad (2)$$

where  $\epsilon_m$  and  $\epsilon_d$  are the permittivities of the alternating layers in the equivalent structure,  $f_m$  and  $f_d$  are the filling fractions, respectively. In the optimization process, the h-BN shell is characterized by the parameters  $\epsilon_m, \epsilon_d, f_m$ , and  $f_d$  of the equivalent structure, and they are dynamically calculated according to the cloaking structure and operating frequency (h-BN is dispersive). The division is fine enough, hence the scattering behavior of the periodic alternating layers is almost the same as that of the h-BN shell before equivalence.

The optimized cylindrical scatterer has a radius of  $\rho_0 = 12.3 \mu\text{m}$ , and the shell has a thickness of  $T = 2.4 \mu\text{m}$ , as

TABLE II. Permittivity model for hexagonal boron nitride (h-BN).

$l$	$\epsilon_l(\infty)$	$s_{v,l}$	$\hbar w_{v,l}/\text{meV}$	$\hbar \gamma_{v,l}/\text{meV}$
$\perp$	4.87	1.83	170.1	0.87
$\parallel$	2.95	0.61	92.5	0.25

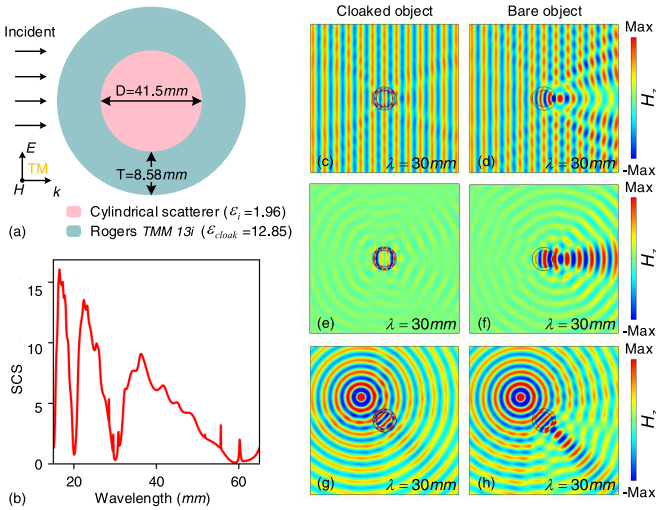


FIG. 3. Multifrequency invisibility properties of the isotropic invisible device. (a) Schematic diagram of the cloaking shell with Rogers *TMM 13i* ( $\epsilon_{\text{cloak}} = 12.85$ ) rolled around the cylindrical scatterer ( $\epsilon_i = 1.96$ ). (b) The relation between the scattering cross section (SCS) and wavelength within the microwave frequency. Numerical simulation results of the  $H_z$  component diagram of the (c) cloaked object and (d) bare object under the excitation of a plane wave. Scattering field diagram of the (e) cloaked object and (f) bare object under the excitation of a plane wave.  $H_z$  component diagram of the (g) cloaked object and (h) bare object under the excitation of a point source. The field diagrams are calculated at the wavelength of 30 mm.

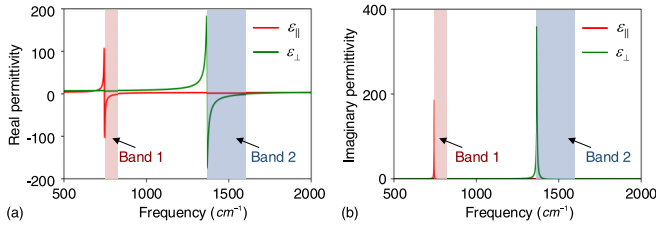


FIG. 4. (a) Real and (b) imaginary parts of the permittivities for h-BN. The different Reststrahlen bands are shaded in different colors.

depicted in Fig. 5(a). The relation between the SCS of the invisible device and the frequency is shown in Fig. 5(b), and the invisibility regime is shaded in grey. It is clearly that the designed invisible device can realize invisibility from 746 to 780  $\text{cm}^{-1}$ , and the bandwidth is almost half of the first Reststrahlen band. Specifically, at the frequency of 746  $\text{cm}^{-1}$ , the in-plane permittivity is  $\varepsilon_{\text{h-BN},\theta} = \varepsilon_{\text{h-BN},z} = \varepsilon_{\text{h-BN},\perp} = 7.4696 + 0.010278i$ , while the out-of-plane permittivity is  $\varepsilon_{\text{h-BN},\rho} = \varepsilon_{\text{h-BN},\parallel} = -82.876 + 185.94i$ . At the frequency of 780  $\text{cm}^{-1}$ , the in-plane permittivity is  $\varepsilon_{\text{h-BN},\theta} = \varepsilon_{\text{h-BN},z} = \varepsilon_{\text{h-BN},\perp} = 7.5757 + 0.011641i$ , while the out-of-plane permittivity is  $\varepsilon_{\text{h-BN},\rho} = \varepsilon_{\text{h-BN},\parallel} = -3.4928 + 0.19259i$ . Even if the permittivity of h-BN varies greatly with the operating frequency, the invisible device performs well in the broad spectral range. To verify the performance of the invisible device, we take the frequency of 746  $\text{cm}^{-1}$  as an example, perform numerical simulations and analytical calculations for the  $H_z$  component diagram. Figures 5(c) and 5(d)

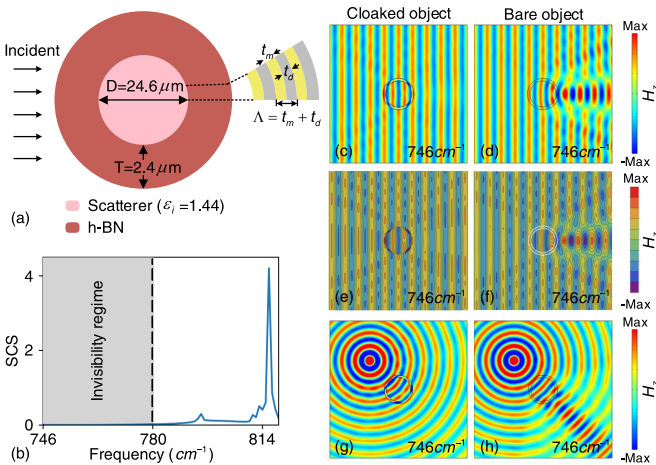


FIG. 5. Invisibility properties of the h-BN invisible device. (a) Schematic diagram of the invisible device with h-BN rolled around the cylindrical scatterer ( $\varepsilon_i = 1.44$ ). (b) The relation between the SCS and frequency within the first Reststrahlen band. The invisibility regime (from 746 to 780  $\text{cm}^{-1}$ ) is shaded in grey. Numerical simulation results of the  $H_z$  component diagram of the (c) cloaked object and (d) bare object under the excitation of a plane wave. Analytical calculation results of the  $H_z$  component diagram of the (e) cloaked object and (f) bare object under the excitation of a plane wave. Numerical simulation results of the  $H_z$  component diagram of the (g) cloaked object and (h) bare object under the excitation of a point source. The field diagrams are calculated at the frequency of 746  $\text{cm}^{-1}$ .

show the numerical simulation results of the  $H_z$  component diagram of the cloaked object under the excitation of a plane wave. Figures 5(e) and 5(f) show the analytical calculation results under the same excitation condition, and the specific analytical calculation for the field distributions can refer to the Appendix. The results of the numerical simulations and analytical calculations are both very accurate and consistent to each other, validating the proposed method can be applied to achieve invisibility in a wider frequency band using vdW materials. Similarly, to further explore the invisibility performance of the hyperbolic invisible device, we change the incident plane wave into a point source and plot the results in Figs. 5(g) and 5(h). It is clearly that when the h-BN is rolled around the cylindrical scatterer, the field distributions are similar to those without any object, as if the cloaked object did not exist. When we perform numerical simulations and analytical calculations, we substitute into the single-layer h-BN shell instead of the 50 periodic metal-dielectric alternating layers after equivalence, and the excellent invisibility performances prove the effectiveness of the proposed effective method. It is worthy to note that this is imperfect invisibility, and we allow the existence of weak scattering in exchange for a wider frequency band. More simulation results of the h-BN invisible device can refer to the Appendix. Furthermore, we take the inherent material losses of h-BN into account in the optimization process to minimize the error between theory and realistic conditions.

The above case strongly demonstrate that the invisibility can be achieved without complex metamaterials, and the design process takes only a fraction of time compared to conventional labor-intensive parameter optimization method. Specifically, on an Intel Core i7-6600U CPU @ 2.90 GHz, the optimization process takes around 6 seconds for the isotropic invisible device, while 4 min and 52 s for the hyperbolic invisible device. The latter takes longer time because the single-layer h-BN shell is equivalent to 50 periodic metal-dielectric alternating layers in the optimization process, hence the calculation process of TMM takes more time. It further illustrates the efficiency of our method.

#### IV. CONCLUSION

In summary, we propose and design the artificial intelligence driven multifrequency isotropic invisible devices and natural hyperbolic invisible devices with a two-layer core-shell configuration. Specifically, we apply EA as a practical tool for the inverse design of invisible devices, which performs global optimization searches directly within the high-dimensional design space, avoiding time-consuming post-processing of the generated designs. Importantly, we demonstrate that the invisible device can be designed using the vdW material h-BN within its first Reststrahlen band through reasonable design, which is innovative in optical field. It is verified that the combination of artificial intelligence and classic electromagnetic theory can be a promising and versatile platform for the design of excellent invisibility phenomena. We envision that this method can be generally utilized to automate the designing process of complex material systems with minimum human intervention.

### ACKNOWLEDGMENTS

The work described here is supported by the Fundamental Research Funds for the National Natural Science Foundation of China (Grants No. 11874311 and No. 92050102), the National Key Research and Development Program of China (Grants No. 2020YFA0710100), the Fundamental Research Funds for the Central Universities (Grants No. 20720220134, No. 20720200074 and No. 20720220033), and the Shenzhen Science and Technology Program (Grants No. JCYJ20210324121610028).

### APPENDIX A: EVOLUTIONARY ALGORITHM (EA)

We use the EA to design the invisible device, which is a subdomain of artificial intelligence. The optimization objective is to minimize the scattering cross section (SCS) at the operating frequencies to achieve invisibility. The optimization variables include the operating wavelength  $\lambda$ , the radius of the cylindrical scatterer  $\rho_0$ , the thickness  $T$  and the relative permittivity  $\varepsilon_{\text{cloak}}$  of the cloaking shell. These optimization variables are defined as the chromosomes of individuals. The optimization process is as follows [48].

Step 1: Initializing a population in the solution space randomly, including 100 individuals, as the initial solutions;

Step 2: The genes of individuals encode the optimization variables with the floating-point encoding method;

Step 3: Calculating the fitness, e.g., the SCS value, of each individual;

Step 4: Following the principle that the higher the fitness, the greater the probability of being selected, to pick the parents that participate in reproduction;

Step 5: Generating the offspring after the crossover, mutation and ranking operations;

Step 6: Updating the fitness of each individual and determining whether the end condition is satisfied. Here the end condition is reproducing for 100 generations;

Step 7: If the end condition is satisfied, outputting the global optimal solution and ending the optimization process; otherwise, turning to Step 4 to continue execution.

In this work, we inversely design the structure and the material of the cloaking shell simultaneously. For structure design, we set the variable range of the cylindrical scatterer radius  $\rho_0$  from  $0.6\lambda$  to  $1.4\lambda$ , where  $\lambda$  is the operating wavelength; and set the variable range of the cloaking shell thickness  $T$  from  $0.1\lambda$  to  $0.5\lambda$ . For material design, we give two examples of isotropic invisible device and hyperbolic invisible device. As for the design of isotropic invisible device, we enter the relative permittivities of the Rogers RF materials into an array, and locate the corresponding material by the index. As for the design of hyperbolic invisible device, we limit the operating frequency  $\omega$  in h-BN's first Reststrahlen band, i.e.,  $746$  to  $819$   $\text{cm}^{-1}$ . As mentioned in the main text, to solve the nonconvergence problem, we set 50 periodic metal-dielectric alternating layers to equivalent the h-BN shell. By calling the `fsolve` function in the `scipy.optimize` package, we calculate the relative permittivities of the alternating layers  $\varepsilon_m$  and  $\varepsilon_d$  dynamically according to the effective medium theory. Then we substitute the equivalent periodic layers into

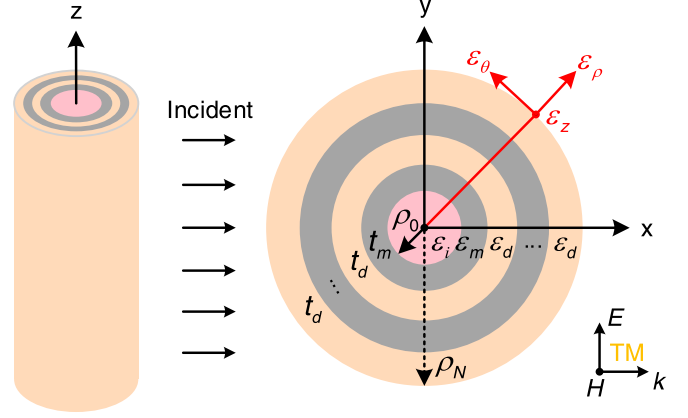


FIG. 6. Illustration of the multilayered cylindrical structure.

the transfer matrix method (TMM) to calculate the SCS and optimize the invisible device with EA.

### APPENDIX B: TRANSFER MATRIX METHOD (TMM)

The TMM is used to calculate the SCS of multilayered cylinders. Although the examples in the main text are the simple two-layer cylindrical structures, for the design of hyperbolic invisible device, the single-layer h-BN shell is equivalent to 50 periodic metal-dielectric alternating layers by applying the effective medium theory. Therefore, to make the discussion more universal, we take the multilayered concentric cylinder as an example, as shown in Fig. 6, and apply TMM to calculate the SCS [49,50].

We assume an incident transverse magnetic (TM) plane wave impinging on the cylindrical structure. The magnetic field of the incident plane wave is expressed as

$$H_{in} = \hat{z}H_0 \sum_{m=-\infty}^{+\infty} i^m J_m(k_0\rho) e^{im\theta}, \quad (\text{B1})$$

where  $\rho$  and  $\theta$  are the radial and azimuthal cylindrical coordinates, respectively.  $H_0$  is a constant amplitude,  $J_m$  is the Bessel function of order  $m$ ,  $k_0 = 2\pi c/\lambda$  is the wave number in vacuum. The scattered magnetic field in the background medium for  $\rho > \rho_N$  can be written as

$$H_{sca} = \hat{z}H_0 \sum_{m=-\infty}^{+\infty} i^m [J_m(k_0\rho) + d_m H_m^{(1)}(k_0\rho)] e^{im\theta}, \quad (\text{B2})$$

where  $H_m^{(1)}$  is the Hankel function of the first kind and order  $m$ . The magnetic field in a given  $n$ th layer ( $\rho_{n-1} < \rho < \rho_n$ ) can be expressed as

$$H_n = \hat{z}H_0 \sum_{m=-\infty}^{+\infty} i^m [b_{m,n} J_m(k_n\rho) + c_{m,n} H_m^{(1)}(k_n\rho)] e^{im\theta}, \quad (\text{B3})$$

where  $k_n = k_0\sqrt{\varepsilon_n}$ . For  $k_i = k_0\sqrt{\varepsilon_i}$ ,  $\varepsilon_i$  represents permittivity of the core medium; the magnetic field in the core of the structure (for  $\rho < \rho_0$ ) can be expressed as

$$H_c = \hat{z}H_0 \sum_{m=-\infty}^{+\infty} i^m a_m J_m(k_i\rho) e^{im\theta}. \quad (\text{B4})$$

The coefficients  $a_m$ ,  $b_m$ ,  $c_m$ , and  $d_m$  are determined by applying boundary conditions for the continuity of tangential electric and magnetic fields between the layers. The boundary conditions between the layers, applied at  $\rho = \rho_n$ , can be expressed in the matrix form as

$$D_{m,n}(\rho_n) \begin{bmatrix} b_{m,n} \\ c_{m,n} \end{bmatrix} = D_{m,n+1}(\rho_n) \begin{bmatrix} b_{m,n+1} \\ c_{m,n+1} \end{bmatrix}, \quad (\text{B5})$$

where the matrix  $D_{m,n}$  can be explained as

$$D_{m,n}(\rho_n) = \begin{bmatrix} J_m(k_n \rho_n) & H_m^{(1)}(k_n \rho_n) \\ \frac{J'_m(k_n \rho_n)}{\sqrt{\varepsilon_n}} & \frac{H_m^{(1)'}(k_n \rho_n)}{\sqrt{\varepsilon_n}} \end{bmatrix}, \quad (\text{B6})$$

where the  $J'_m$  and  $H_m^{(1)'}$  denote the derivatives. We also define a matrix  $T_m$  as

$$T_m = \begin{bmatrix} T_{m,11} & T_{m,12} \\ T_{m,21} & T_{m,22} \end{bmatrix}, \quad (\text{B7})$$

$$T_m = D_{m,1}(\rho_0) \left\{ \prod_{n=1}^N [D_{m,n}(\rho_n)]^{-1} D_{m,n+1}(\rho_n) \right\}. \quad (\text{B8})$$

We can relate the scattering coefficient as

$$d_m = \frac{xT_{m,21} - yT_{m,11}}{yT_{m,12} - xT_{m,22}}, \quad (\text{B9})$$

where  $x = J_m(k_n \rho_n)$  and  $y = J'_m(k_n \rho_n) / \sqrt{\varepsilon_n}$ . Finally, the SCS is expressed as

$$\sigma = \sum_{m=-\infty}^{+\infty} |d_m|^2. \quad (\text{B10})$$

#### APPENDIX C: ANALYTICAL CALCULATION FOR FIELD DISTRIBUTIONS WITH ANISOTROPIC MATERIALS

To better demonstrate our numerical results, we analytically calculate for the field distributions. The general wave equation that governs the TM field ( $H_z$ ) along the  $z$  axis can be written as

$$r^2 \frac{\partial^2 H_z}{\partial r^2} + r \frac{\partial H_z}{\partial r} + (k^2 r^2 - \tilde{m}^2) H_z = 0, \quad (\text{C1})$$

where  $r$  is the distance from the center of the rod,  $k = k_0 \sqrt{\varepsilon_\theta}$  and  $\tilde{m} = m \sqrt{\varepsilon_\theta / \varepsilon_\rho}$  ( $m$  is an integer). For isotropic materials such as air or medium,  $\varepsilon_\theta = \varepsilon_\rho$  and  $\tilde{m} = m$ . For hyperbolic materials such as h-BN,  $\varepsilon_\theta \neq \varepsilon_\rho$  and  $\tilde{m} \neq m$ , and  $\tilde{m}$  may be a complex number.

As shown in Fig. 3(a) in the main text, for the isotropy region ( $r < \rho_0$  and  $r > \rho_0 + T$ ), the general solution of wave equation can be expressed as

$$H_z = \sum_{m=-\infty}^{+\infty} [A_m J_m(k_0 r) + B_m H_m^{(1)}(k_0 r)] e^{im\theta} \quad (r > \rho_0 + T),$$

$$H_z = \sum_{m=-\infty}^{+\infty} D_m J_m(k_0 \sqrt{\varepsilon_\theta} r) e^{im\theta} \quad (r < \rho_0, \varepsilon_\theta = \varepsilon_i), \quad (\text{C2})$$

where  $J_m(k_0 r)$  is the Bessel functions and  $H_m^{(1)}(k_0 r)$  is the Hankel functions of the first kind. For the hyperbolic region

( $\rho_0 < r < \rho_0 + T$ ), the general solution can be expressed as

$$H_z = \sum_{m=-\infty}^{+\infty} [C_{1m} J_{\tilde{m}}(k_0 \sqrt{\varepsilon_\theta} r) + C_{2m} H_{\tilde{m}}^{(1)}(k_0 \sqrt{\varepsilon_\theta} r)] e^{im\theta}, \quad (\text{C3})$$

where  $A_m$ ,  $B_m$ ,  $C_{1m}$ ,  $C_{2m}$ , and  $D_m$  are complex coefficients. By matching the continual boundary conditions, these coefficients can be further determined.

#### APPENDIX D: REASONS FOR USING EA TO DESIGN INVISIBLE DEVICES

As mentioned before, EA is a subdomain of artificial intelligence. Besides it, there are many other algorithms under the umbrella of artificial intelligence, among which deep learning is the most popular one. Deep learning uses artificial neural networks (ANNs) for data-driven predictions, and it has been employed to design invisible devices in recent years [25,51]. In these works, the ANNs are trained to learn the intrinsic relation between the parameters of the invisible device (such as structure and material properties) and their scattering properties, and they can design the invisible devices immediately after the training phase. However, the design process of ANNs is time-consuming and computationally expensive, involving hyperparameter optimization, training data generation, and extensive testing. And being a data-driven approach, an inevitable forward-modeling error is inherent to deep learning [52]. Additionally, while the ANNs are good at interpolating complex functions from training data, their performance is reduced when extrapolating outside of the known parameter space [22], and it makes the deep learning have limitations in processing complicated problems. Furthermore, once a neural network is trained, it can only be used to solve problems with specific optimization variables, which is very inflexible for the problems to be solved in this work. For example, if there is an ANN trained to design the invisible devices in a two-layer cylindrical structure, and we want to make it suitable for a four-layer cylindrical structure, it is necessary to reprepare the data set, readjust the network structure, and retrain the network. To explore efficient invisible device designs, we choose an EA as the optimization technique due to its ease of implementation, efficiency in exploring a large parameter space, and ability to trace intermediate solutions. Compared with deep learning, EA avoids time-consuming data preparation and is immune to the forward-modeling error. Due to these advantages, EA has been applied to a series of optical researches [26,27]. For example, Conkey *et al.* focused light through turbid media in noisy environments with EA [27]. Our research also shows that EA is very suitable for the design of invisible devices.

#### APPENDIX E: MORE SIMULATION RESULTS OF H-BN INVISIBLE DEVICE

Here we show more simulation results to further verify the broadband invisibility performance of the h-BN invisible device shown in Fig. 5(a) in the main text. Figures 7(a)–7(c) and 7(f)–7(h) show the numerical simulation results of the cloaked object at different frequencies, Figs. 7(d) and 7(i) show the numerical simulation results of the all scatterer

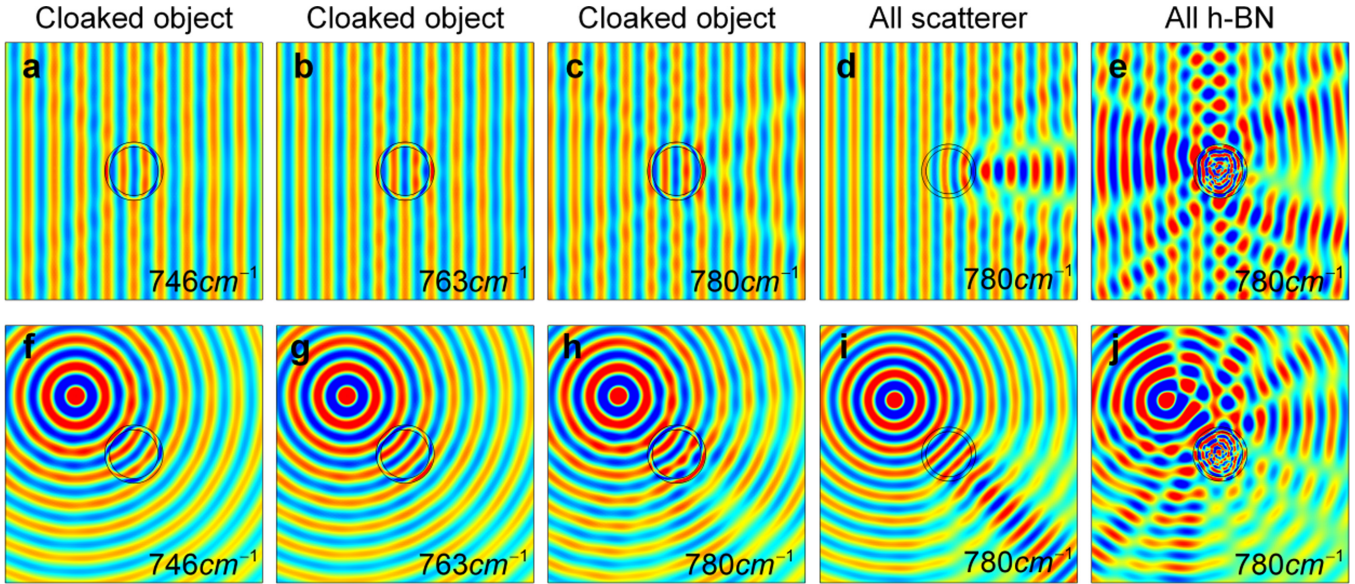


FIG. 7. Numerical simulation results of the  $H_z$  component diagram of the cloaked object under the excitation of a plane wave at the frequency of (a)  $746\text{ cm}^{-1}$ , (b)  $763\text{ cm}^{-1}$ , and (c)  $780\text{ cm}^{-1}$ . Numerical simulation results of the  $H_z$  component diagram of the (d) all scatterer cylinder ( $\epsilon_i = 1.44$ ) and (e) all h-BN cylinder under the excitation of a plane wave at the frequency of  $780\text{ cm}^{-1}$ . Numerical simulation results of the  $H_z$  component diagram of the cloaked object under the excitation of a point source at the frequency of (f)  $746\text{ cm}^{-1}$ , (g)  $763\text{ cm}^{-1}$ , and (h)  $780\text{ cm}^{-1}$ . Numerical simulation results of the  $H_z$  component diagram of the (i) all scatterer cylinder and (j) all h-BN cylinder under the excitation of a point source at the frequency of  $780\text{ cm}^{-1}$ .

structure ( $\epsilon_i = 1.44$ ), and Figs. 7(e) and 7(j) show that of the all h-BN structure. It can be seen that the field distribution is almost undisturbed with the presence of the cloaked object, whereas the incident wave is severely distorted in the case of all scatterer or all h-BN cylinder. It further verifies the validity and rationality of our proposed method.

**APPENDIX F: MORE EXAMPLES FOR INVISIBLE DEVICE DESIGNS**

To prove that our method can provide multiple cloaking shell design schemes for the same core, and can be applied to design cloaking shells for any given core materials, we give more examples here.

First, let us consider the case of isotropic Rogers RF material. For the same core material as presented in the main text  $\epsilon_i = 1.96$ , this method can prove multiple cloaking shell design schemes, and here we show another one of them. As depicted in Fig. 8(e), the optimized cylindrical scatterer has a radius of  $\rho_0 = 20.9\text{ mm}$ , the shell has a thickness of  $T = 9.8\text{ mm}$  with the Rogers RO3010<sup>TM</sup> material ( $\epsilon_{\text{cloak}} = 10.2 - 0.0022i$ ), and the best invisibility performance appears at the wavelength of  $30\text{ mm}$ . To verify the effectiveness of the designed invisible device, we perform full-wave numerical simulations and plot the results in Figs. 8(b)–8(d), which show great invisibility performance.

Then we change the relative permittivity of the core material to  $\epsilon_i = 1.45$ , and continue to optimize the invisible device with EA. As depicted in Fig. 9(a), the optimized

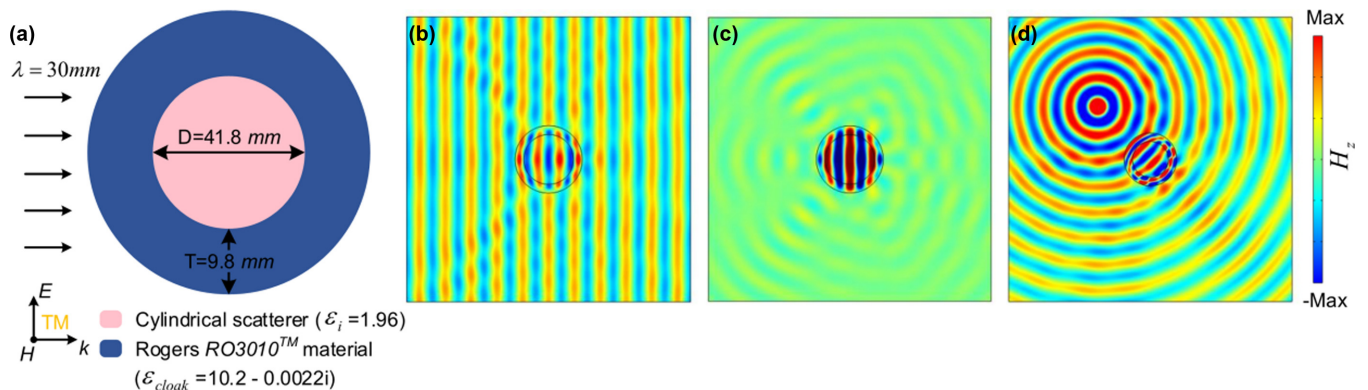


FIG. 8. (a) Schematic diagram of the cloaking shell with Rogers RO3010<sup>TM</sup> material ( $\epsilon_{\text{cloak}} = 10.2 - 0.0022i$ ) rolled around the cylindrical scatterer ( $\epsilon_i = 1.96$ ). Numerical simulations of (b) the  $H_z$  component diagram and (c) the scattering field diagram of the cloaked object under the excitation of a plane wave; (d) the  $H_z$  component diagram of the cloaked object under the excitation of a point source.



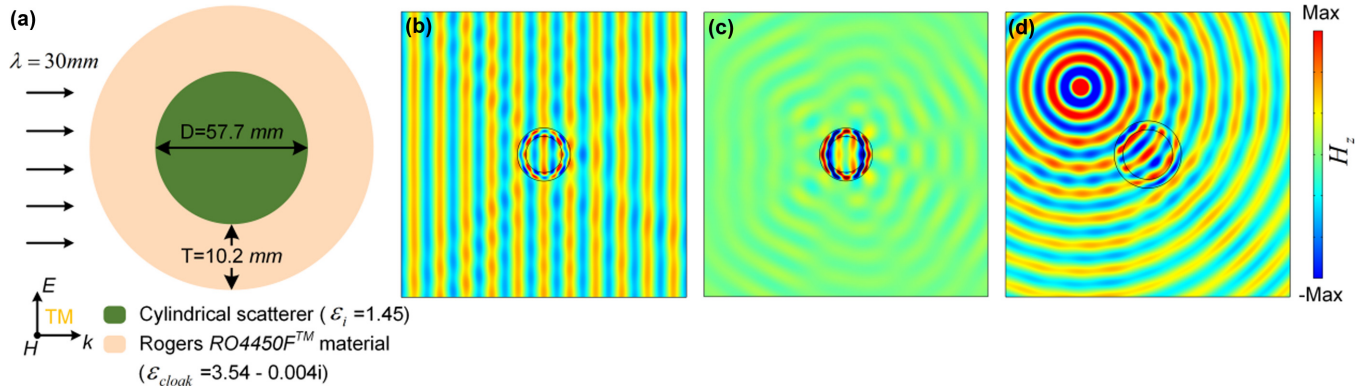


FIG. 9. (a) Schematic diagram of the cloaking shell with Rogers  $RO4450F^{TM}$  material ( $\epsilon_{cloak} = 3.54 - 0.004i$ ) rolled around the cylindrical scatterer ( $\epsilon_i = 1.45$ ). Numerical simulations of (b) the  $H_z$  component diagram and (c) the scattering field diagram of the cloaked object under the excitation of a plane wave; (d) the  $H_z$  component diagram of the cloaked object under the excitation of a point source.

cylindrical scatterer has a radius of  $\rho_0 = 28.8$  mm, the shell has a thickness of  $T = 10.2$  mm with the Rogers  $RO4450F^{TM}$  material ( $\epsilon_{cloak} = 3.54 - 0.004i$ ), and the best invisibility

performance appears at the wavelength of 30 mm. As shown in Figs. 9(b)–9(d), the designed invisible device has good invisibility performance as well.

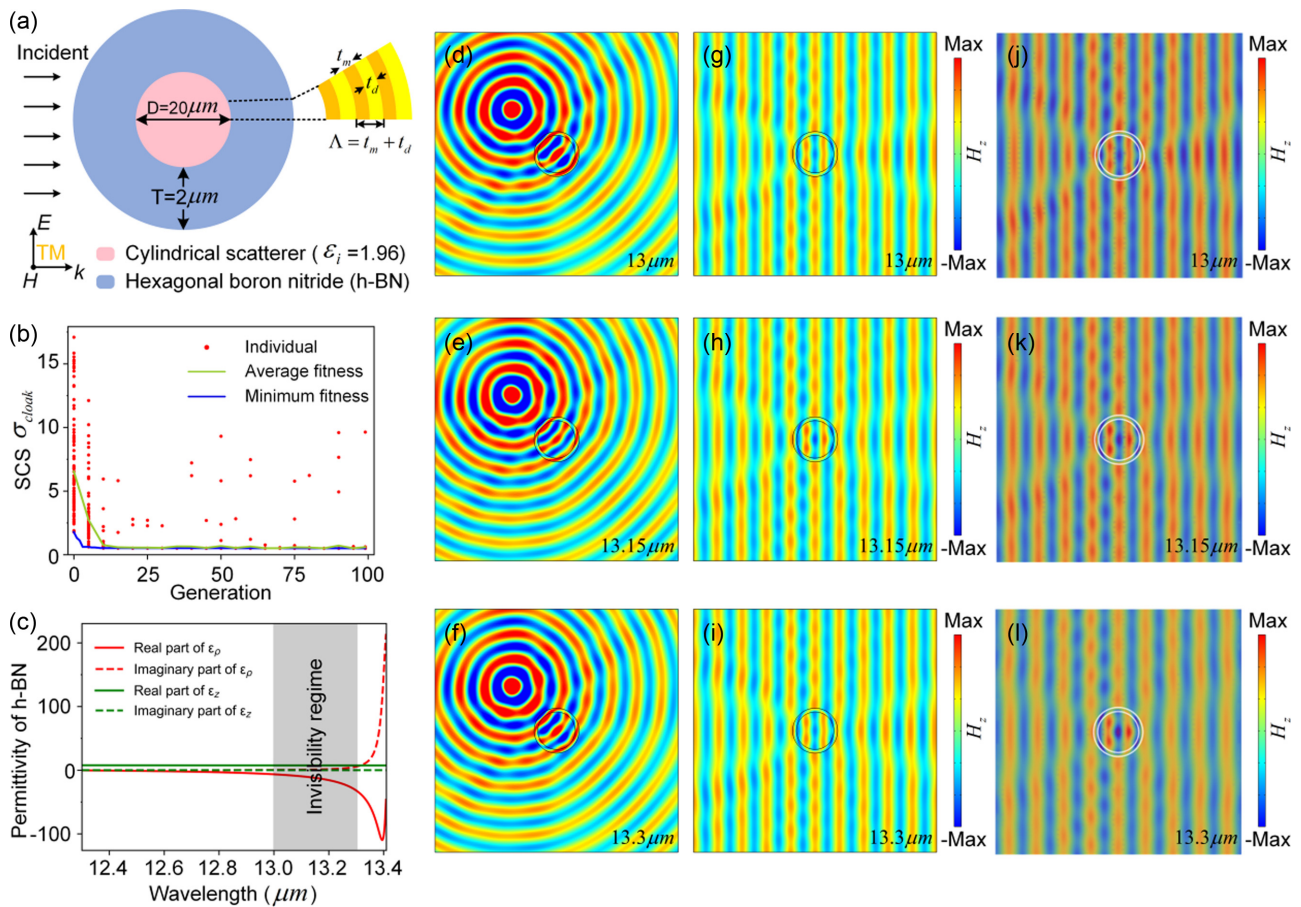


FIG. 10. (a) Schematic diagram of the cloaking shell with hexagonal boron nitride (h-BN) rolled around the cylindrical scatterer ( $\epsilon_i = 1.96$ ) and the corresponding periodic metal-dielectric alternating layers. (b) The population fitness, e.g., the SCS of the cloaked object, of 100 generations. (c) The relation between the real and imaginary part of the permittivity for h-BN and the wavelength  $\lambda$ . The gray area is the broadband invisibility regime. Numerical simulations of the  $H_z$  component diagram of the cloaked object under the excitation of a point source at the wavelength of (d)  $13 \mu\text{m}$ , (e)  $13.15 \mu\text{m}$ , and (f)  $13.3 \mu\text{m}$ ; under the excitation of a plane wave at the wavelength of (g)  $13 \mu\text{m}$ , (h)  $13.15 \mu\text{m}$ , and (i)  $13.3 \mu\text{m}$ . Analytical calculations of  $H_z$  component diagram of the cloaked object under the excitation of a plane wave at the wavelength of (j)  $13 \mu\text{m}$ , (k)  $13.15 \mu\text{m}$ , and (l)  $13.3 \mu\text{m}$ .

Second, let us verify the effectiveness of h-BN invisible device for different core materials. We set the relative permittivity of the core to ( $\varepsilon_i = 1.96$ ), and continue to optimize the invisible device with EA for 100 generations. It can be seen from Fig. 10(b) that the individuals converge to the optimal solution after about 10 generations. The optimized cylindrical scatterer has a radius of  $\rho_0 = 10 \mu\text{m}$ , and the shell has a thickness of  $T = 2 \mu\text{m}$  [Fig. 10(a)]. The designed invisible device can achieve invisibility at the operating wavelength from  $13 \mu\text{m}$  to  $13.3 \mu\text{m}$  [Fig. 10(c)]. Here we perform numerical simulations and analytical calculations for the  $H_z$  component diagram of the cloaked object at three operating wavelength of  $13 \mu\text{m}$ ,  $13.15 \mu\text{m}$  and  $13.3 \mu\text{m}$ , as shown in Figs. 10(d)–10(l). Specifically, at the wavelength of  $13 \mu\text{m}$ , the principle permittivity in the  $\rho$  direction is  $\varepsilon_{\text{h-BN},\rho} =$

$-6.478 - 0.407i$ , while the principle permittivity in the  $\theta$  direction and  $z$  direction is  $\varepsilon_{\text{h-BN},\theta} = \varepsilon_{\text{h-BN},z} = 7.541 - 0.011i$ . At the wavelength of  $13.15 \mu\text{m}$ , the principle permittivity in the  $\rho$  direction is  $\varepsilon_{\text{h-BN},\rho} = -12.068 - 1.024i$ , while the principle permittivity in the  $\theta$  direction and  $z$  direction is  $\varepsilon_{\text{h-BN},\theta} = \varepsilon_{\text{h-BN},z} = 7.513 - 0.0108i$ . At the wavelength of  $13.3 \mu\text{m}$ , the principle permittivity in the  $\rho$  direction is  $\varepsilon_{\text{h-BN},\rho} = -31.851 - 5.549i$ , while the principle permittivity in the  $\theta$  direction and  $z$  direction is  $\varepsilon_{\text{h-BN},\theta} = \varepsilon_{\text{h-BN},z} = 7.487 - 0.0104i$ . The results show that although the permittivity of h-BN varies greatly with the operating wavelength, the h-BN invisible device has excellent equivalent performance in a broad spectral range. This case further demonstrates that our method can be applied to design h-BN invisible devices for any given core materials.

- 
- [1] C. Qian and H. Chen, A perspective on the next generation of invisibility cloaks—Intelligent cloaks, *Appl. Phys. Lett.* **118**, 180501 (2021).
- [2] J. B. Pendry, D. Schurig, and D. R. Smith, Controlling electromagnetic fields, *Science* **312**, 1780 (2006).
- [3] U. Leonhardt, Optical conformal mapping, *Science* **312**, 1777 (2006).
- [4] H. Chen, C. T. Chan, and P. Sheng, Transformation optics and metamaterials, *Nat. Mater.* **9**, 387 (2010).
- [5] J. Li and J. B. Pendry, Hiding Under the Carpet: A New Strategy for Cloaking, *Phys. Rev. Lett.* **101**, 203901 (2008).
- [6] R. Liu, C. Ji, J. Mock, J. Chin, T. Cui, and D. Smith, Broadband ground-plane cloak, *Science* **323**, 366 (2009).
- [7] J. Valentine, J. Li, T. Zentgraf, G. Bartal, and X. Zhang, An optical cloak made of dielectrics, *Nat. Mater.* **8**, 568 (2009).
- [8] L. H. Gabrielli, J. Cardenas, C. B. Poitras, and M. Lipson, Silicon nanostructure cloak operating at optical frequencies, *Nat. Photon.* **3**, 461 (2009).
- [9] Y. Lai, J. Ng, H. Y. Chen, D. Z. Han, J. J. Xiao, Z.-Q. Zhang, and C. T. Chan, Illusion Optics: The Optical Transformation of an Object into Another Object, *Phys. Rev. Lett.* **102**, 253902 (2009).
- [10] C. Li, X. Meng, X. Liu, F. Li, G. Fang, H. Chen, and C. T. Chan, Experimental Realization of a Circuit-Based Broadband Illusion-Optics Analogue, *Phys. Rev. Lett.* **105**, 233906 (2010).
- [11] K.-P. Ye, W.-J. Pei, Z.-H. Sa, H. Chen, and R.-X. Wu, Invisible Gateway by Superscattering Effect of Metamaterials, *Phys. Rev. Lett.* **126**, 227403 (2021).
- [12] H. Chen and C. Chan, Transformation media that rotate electromagnetic fields, *Appl. Phys. Lett.* **90**, 241105 (2007).
- [13] H. Chen, B. Hou, S. Chen, X. Ao, W. Wen, and C. T. Chan, Design and Experimental Realization of a Broadband Transformation Media Field Rotator at Microwave Frequencies, *Phys. Rev. Lett.* **102**, 183903 (2009).
- [14] M. Rahm, D. Schurig, D. A. Roberts, S. A. Cummer, D. R. Smith, and J. B. Pendry, Design of electromagnetic cloaks and concentrators using form-invariant coordinate transformations of maxwells equations, *Photon. Nanostruct. Fund. Appl.* **6**, 87 (2008).
- [15] M. Sadeghi, S. Li, L. Xu, B. Hou, and H. Chen, Transformation optics with Fabry-Pérot resonances, *Sci. Rep.* **5**, 1 (2015).
- [16] R. Fleury and A. Alu, Cloaking and invisibility: A review, *Prog. Electromagn. Res.* **147**, 171 (2014).
- [17] B. Zhang, H. Chen, and B.-I. Wu, Practical limitations of an invisibility cloak, *Prog. Electromagn. Res.* **97**, 407 (2009).
- [18] S. A. Cummer, B.-I. Popa, D. Schurig, D. R. Smith, and J. Pendry, Full-wave simulations of electromagnetic cloaking structures, *Phys. Rev. E* **74**, 036621 (2006).
- [19] D. Schurig, J. J. Mock, B. Justice, S. A. Cummer, J. B. Pendry, A. F. Starr, and D. R. Smith, Metamaterial electromagnetic cloak at microwave frequencies, *Science* **314**, 977 (2006).
- [20] W. Cai, U. K. Chettiar, A. V. Kildishev, V. M. Shalaev, and G. W. Milton, Nonmagnetic cloak with minimized scattering, *Appl. Phys. Lett.* **91**, 111105 (2007).
- [21] W. Cai, U. K. Chettiar, A. V. Kildishev, and V. M. Shalaev, Optical cloaking with metamaterials, *Nat. Photon.* **1**, 224 (2007).
- [22] A. Alù and N. Engheta, Achieving transparency with plasmonic and metamaterial coatings, *Phys. Rev. E* **72**, 016623 (2005).
- [23] A. Alù and N. Engheta, Multifrequency Optical Invisibility Cloak with Layered Plasmonic Shells, *Phys. Rev. Lett.* **100**, 113901 (2008).
- [24] B. Wu, Z.-L. Hao, J.-H. Chen, Q.-L. Bao, Y.-N. Liu, and H.-Y. Chen, Total transmission from deep learning designs, *J. Electron. Sci. Technol.* **20**, 100146 (2022).
- [25] W. W. Ahmed, M. Farhat, X. Zhang, and Y. Wu, Deterministic and probabilistic deep learning models for inverse design of broadband acoustic cloak, *Phys. Rev. Res.* **3**, 013142 (2021).
- [26] J. C. Forster, J. Krausser, M. R. Vuyyuru, B. Baum, and A. Šarić, Exploring the Design Rules for Efficient Membrane-Reshaping Nanostructures, *Phys. Rev. Lett.* **125**, 228101 (2020).
- [27] D. B. Conkey, A. N. Brown, A. M. Caravaca-Aguirre, and R. Piestun, Genetic algorithm optimization for focusing through turbid media in noisy environments, *Opt. Express* **20**, 4840 (2012).
- [28] W. Ma, B. Shabbir, Q. Ou, Y. Dong, H. Chen, P. Li, X. Zhang, Y. Lu, and Q. Bao, Anisotropic polaritons in van der Waals materials, *InfoMat* **2**, 777 (2020).
- [29] Z. Zheng, N. Xu, S. L. Oscurato, M. Tamagnone, F. Sun, Y. Jiang, Y. Ke, J. Chen, W. Huang, W. L. Wilson *et al.*, A

- mid-infrared biaxial hyperbolic van der Waals crystal, *Sci. Adv.* **5**, eaav8690 (2019).
- [30] D. R. Smith and D. Schurig, Electromagnetic Wave Propagation in Media with Indefinite Permittivity and Permeability Tensors, *Phys. Rev. Lett.* **90**, 077405 (2003).
- [31] A. Poddubny, I. Iorsh, P. Belov, and Y. Kivshar, Hyperbolic metamaterials, *Nat. Photon.* **7**, 948 (2013).
- [32] S. Dai, Z. Fei, Q. Ma, A. Rodin, M. Wagner, A. McLeod, M. Liu, W. Gannett, W. Regan, K. Watanabe *et al.*, Tunable phonon polaritons in atomically thin van der Waals crystals of boron nitride, *Science* **343**, 1125 (2014).
- [33] J. D. Caldwell, A. V. Kretinin, Y. Chen, V. Giannini, M. M. Fogler, Y. Francescato, C. T. Ellis, J. G. Tischler, C. R. Woods, A. J. Giles *et al.*, Sub-diffractive volume-confined polaritons in the natural hyperbolic material hexagonal boron nitride, *Nat. Commun.* **5**, 5221 (2014).
- [34] P. Li, I. Dolado, F. J. Alfaro-Mozaz, F. Casanova, L. E. Hueso, S. Liu, J. H. Edgar, A. Y. Nikitin, S. Vélez, and R. Hillenbrand, Infrared hyperbolic metasurface based on nanostructured van der Waals materials, *Science* **359**, 892 (2018).
- [35] W. Ma, P. Alonso-González, S. Li, A. Y. Nikitin, J. Yuan, J. Martín-Sánchez, J. Taboada-Gutiérrez, I. Amenabar, P. Li, S. Vélez *et al.*, In-plane anisotropic and ultra-low-loss polaritons in a natural van der Waals crystal, *Nature (London)* **562**, 557 (2018).
- [36] J. Taboada-Gutiérrez, G. Álvarez-Pérez, J. Duan, W. Ma, K. Crowley, I. Prieto, A. Bylinkin, H. Volkova, K. Kimura, T. Kimura *et al.*, Broad spectral tuning of ultra-low-loss polaritons in a van der Waals crystal by intercalation, *Nat. Mater.* **19**, 964 (2020).
- [37] A. Sternbach, S. Chae, S. Latini, A. Rikhter, Y. Shao, B. Li, D. Rhodes, B. Kim, P. J. Schuck, X. Xu *et al.*, Programmable hyperbolic polaritons in van der Waals semiconductors, *Science* **371**, 617 (2021).
- [38] F. Alfaro-Mozaz, P. Alonso-González, S. Vélez, I. Dolado, S. Mastel, F. Casanova, L. E. Hueso, P. Li, A. Y. Nikitin, R. Hillenbrand *et al.*, Nanoimaging of resonating hyperbolic polaritons in linear boron nitride antennas, *Nat. Commun.* **8**, 15624 (2017).
- [39] A. J. Giles, S. Dai, I. Vurgaftman, T. Hoffman, S. Liu, L. Lindsay, C. T. Ellis, N. Assefa, I. Chatzakis, T. L. Reinecke *et al.*, Ultralow-loss polaritons in isotopically pure boron nitride, *Nat. Mater.* **17**, 134 (2018).
- [40] K. S. Novoselov, D. Jiang, F. Schedin, T. Booth, V. Khotkevich, S. Morozov, and A. K. Geim, Two-dimensional atomic crystals, *Proc. Natl. Acad. Sci. USA* **102**, 10451 (2005).
- [41] C. Qian, X. Lin, Y. Yang, F. Gao, Y. Shen, J. Lopez, I. Kaminer, B. Zhang, E. Li, M. Soljacic *et al.*, Multifrequency superscattering from subwavelength hyperbolic structures, *ACS Photon.* **5**, 1506 (2018).
- [42] B. Liu, X. Zhang, J. Du, J. Xiao, H. Yu, M. Hong, L. Gao, Y. Ou, Z. Kang, Q. Liao *et al.*, Synergistic-engineered van der Waals photodiodes with high efficiency, *InfoMat* **4**, e12282 (2022).
- [43] P. Li, M. Lewin, A. V. Kretinin, J. D. Caldwell, K. S. Novoselov, T. Taniguchi, K. Watanabe, F. Gaussmann, and T. Taubner, Hyperbolic phonon-polaritons in boron nitride for near-field optical imaging and focusing, *Nat. Commun.* **6**, 1 (2015).
- [44] K.-J. Tielrooij, N. C. Hesp, A. Principi, M. B. Lundeberg, E. A. Pogna, L. Banszerus, Z. Mics, M. Massicotte, P. Schmidt, D. Davydovskaya *et al.*, Out-of-plane heat transfer in van der Waals stacks through electron-hyperbolic phonon coupling, *Nat. Nanotechnol.* **13**, 41 (2018).
- [45] G. Hu, Q. Ou, G. Si, Y. Wu, J. Wu, Z. Dai, A. Krasnok, Y. Mazor, Q. Zhang, Q. Bao *et al.*, Topological polaritons and photonic magic angles in twisted  $\alpha$ -moo<sub>3</sub> bilayers, *Nature (London)* **582**, 209 (2020).
- [46] T. Hou, S. Tao, H. Mu, Q. Bao, and H. Chen, Invisibility concentrator based on van der Waals semiconductor  $\alpha$ -moo<sub>3</sub>, *Nanophotonics* **11**, 369 (2022).
- [47] A. Woessner, M. B. Lundeberg, Y. Gao, A. Principi, P. Alonso-González, M. Carrega, K. Watanabe, T. Taniguchi, G. Vignale, M. Polini *et al.*, Highly confined low-loss plasmons in graphene-boron nitride heterostructures, *Nat. Mater.* **14**, 421 (2015).
- [48] M. Affenzeller, S. Wagner, S. Winkler, and A. Beham, *Genetic Algorithms and Genetic Programming: Modern Concepts and Practical Applications* (Chapman and Hall/CRC, London, UK, 2009).
- [49] C. F. Bohren and D. R. Huffman, *Absorption and Scattering of Light by Small Particles* (John Wiley & Sons, New York, NY, 2008).
- [50] C. Díaz-Aviñó, M. Naserpour, and C. J. Zapata-Rodríguez, Optimization of multilayered nanotubes for maximal scattering cancellation, *Opt. Express* **24**, 18184 (2016).
- [51] C. Qian, B. Zheng, Y. Shen, L. Jing, E. Li, L. Shen, and H. Chen, Deep-learning-enabled self-adaptive microwave cloak without human intervention, *Nat. Photon.* **14**, 383 (2020).
- [52] P. R. Wiecha and O. L. Muskens, Deep learning meets nanophotonics: A generalized accurate predictor for near fields and far fields of arbitrary 3D nanostructures, *Nano Lett.* **20**, 329 (2020).